A&A, 689, A307 (2024)
https://doi.org/10.1051/0004-6361/202450315

Astronomy & Astrophysics

Markov chain Monte Carlo inversions of the internal rotation of *Kepler* subgiants

G. Buldgen[1,2,⋆], L. Fellay[1], J. Bétrisey[2], S. Deheuvels[3], M. Farnir[1], and E. Farrell[2]

[1] STAR Institute, Université de Liège, Liège, Belgium
[2] Département d'Astronomie, Université de Genève, Chemin Pegasi 51, 1290 Versoix, Switzerland
[3] IRAP, Université de Toulouse, CNRS, CNES, UPS, 14 avenue Edouard Belin, 31400 Toulouse, France

Received 10 April 2024 / Accepted 9 May 2024

ABSTRACT

Context. The measurement of the internal rotation of post-main-sequence stars using data from space-based photometry missions has demonstrated the need for an efficient angular momentum transport in stellar interiors. No clear solution has emerged so far, and it remains a challenge for stellar modellers to explain the observed trends.
Aims. We constrained the shape of the internal rotation profile of six *Kepler* subgiants that were studied in details in 2014 and also the properties of the missing angular momentum transport process that acts in stellar interiors from Markov chain Monte Carlo (MCMC) inversions of the internal rotation.
Methods. We applied a new MCMC inversion technique to existing *Kepler* subgiant targets and tested various shapes of the internal rotation profile of the six subgiants that were observed in 2014. We also constrained the limitations on the number of free parameters that can be used in the MCMC inversion, showing the limitations in the amount of information in the seismic data.
Results. First, we show that large-scale fossil magnetic fields are not able to explain the internal rotation of subgiants, similarly to what was determined from detailed studies of *Kepler* red giants. We are also able to constrain the location of the transition in the internal rotation profile for the most evolved stars in the available set of subgiants. We find that some of them exhibit a transition that is located close to the border of the helium core, but one object exhibit a transition located much higher in radius.
Conclusions. We conclude that various processes might be at play that would explain our observations, but a consistent detailed modelling of all available subgiants is required to reveal the physical nature of the angular momentum process, in particular, for the least evolved objects. In addition, it is paramount to increase the number of stars for which these inferences are possible (e.g. with the future PLATO mission) because they play a key role in validating candidates for the transport process.

Key words. asteroseismology – stars: evolution – stars: interiors – stars: rotation

1. Introduction

With the advent of space-based photometry missions such as CoRoT (Auvergne et al. 2009), *Kepler* (Borucki et al. 2010), and TESS (Ricker et al. 2015), stellar modellers gained direct access to constraints on the internal rotation of post-main-sequence stars. Further data are expected to be made available with the future PLATO mission (Rauer et al. 2014). This was made possible by the observations of so-called mixed oscillation modes, which present a dual nature of the gravity and acoustic modes, and in this way, contain information on the innermost layers of these stars. Inference results (e.g. Beck et al. 2012; Deheuvels et al. 2012, 2014, 2015, 2020; Mosser et al. 2012; Di Mauro et al. 2016, 2018; Gehan et al. 2018; Fellay et al. 2021 have provided direct evidence that an efficient angular momentum transport process acts in stellar radiative zones. Stellar evolution models have proven unable to reproduce these constraints (Marques et al. 2013) even when classical solutions that were put forward to reproduce the internal rotation of the Sun were introduced in the equation for the angular momentum transport (Gough & McIntyre 1998; Spruit 2002; Charbonnel & Talon 2005). Various candidates were put forward, but none of them was able to provide a full solution (Aerts et al. 2019).

An interesting feature of these various candidates is the shape of the internal rotation profile they would induce. For example, fossil magnetic fields as introduced by Kissin & Thompson (2015) and tested by Takahashi & Langer (2021) would leave a solid-body rotation in the radiative zone, followed by a power law in radius in the outer convective envelope. Similarly, internal gravity waves and magnetic instabilities would be hindered by gradients in the mean molecular weight. Therefore, the transition from the slowly rotating envelope to the fast-rotating core in their internal rotation profile is expected to be located close to regions with strong chemical gradients (see e.g. Maeder 2009, for a classical textbook on the topic).

In subgiant and red giant stars, these regions are found at the border of the helium core and the hydrogen shell. Therefore, some favoured shapes of rotation profiles can be tested and optimised to validate or invalidate the physical nature of the missing mechanism for the angular momentum transport. Attempts were made for red giant branch stars in Di Mauro et al. (2016), Di Mauro et al. (2018), Fellay et al. (2021), and Wilson et al. (2023) on one of the subgiants studied here. While the former two privileged a transition located close to the hydrogen shell, the latter used an independent surface rotation by García et al. (2014) to test a two-zone model and to weakly constrain the location of the transition in rotation under 0.4 normalised radii. Markov Chain Monte Carlo (MCMC) inversions

⋆ Corresponding author; gbuldgen@uliege.be

Table 1. Global parameters of the CESAM2K stellar evolution models from Deheuvels et al. (2014).

Name	KIC	$M/M_\odot$	Age (Gyr)	$R/R_\odot$	$(Z/X)_0$	Y_0
Star A	KIC 12508433	1.22	5.9	2.231	0.0500	0.30
Star B	KIC 8702606	1.27	3.8	2.467	0.0173	0.27
Star C	KIC 5689820	1.14	6.9	2.297	0.0388	0.30
Star D	KIC 8751420	1.26	3.8	2.670	0.0151	0.27
Star E	KIC 7799349	1.39	3.8	2.829	0.0548	0.30
Star F	KIC 9574283	1.07	6.0	2.793	0.0116	0.27

were also applied to KIC11145123 in Hatta et al. (2022), which confirmed the SOLA inversions they carried out in a previous publication (Hatta et al. 2019).

In this paper, we extend the experiment to the entire set of subgiant stars studied by Deheuvels et al. (2014), using the original models and multiple shapes of reference rotation profiles. We start by briefly recalling the properties of the models in Sect. 2, then we carry out SOLA inversions in Sect 3 and compare our results to those of Deheuvels et al. (2014). In Sect 4, we carry out an extensive analysis using MCMC inversions first on artificial data and then on the observed splittings. We also discuss the properties of the profiles. In Sect. 5, we discuss our findings and the implications for the angular momentum transport process acting on the subgiant branch and the limitations of our approach. We conclude and provide some additional perspectives in Sect. 6.

2. Stellar models

The stellar models used in this study are the CESAM2K models of Deheuvels et al. (2014). The oscillation frequencies and rotation kernels were computed using the ADIPLS oscillation package (Christensen-Dalsgaard 2011). We summarise their global properties in Table 1. An interesting property of all the stars in this sample is that their masses are quite similar, which allowed us to analyse their rotation properties in an almost purely evolutionary context. However, stars E and F cannot be analysed in such a way, as the former did not harbour a convective core during the main sequence and the latter is at the other extreme of the considered mass range.

The set of models can already be separated in three groups, with the somewhat younger subgiants being star A and B, C and D being in relatively intermediate stages and star E and F being already at the bottom of the RGB or starting to climb it. Due to the detailed modelling procedure carried out in Deheuvels et al. (2014), we can consider that these models are suitable to compute rotation inversions.

As all these stars are slow-rotators, the effects of rotation can be treated as a first order perturbation to the non-rotating solution. In this case, the so-called rotation splittings, $\delta\nu^m_{n,\ell}$, are linked to the internal rotation profile, Ω, by the following equation (Hansen et al. 1977; Gough 1981)

$$\delta\nu^m_{n,\ell} = m\int_0^R K_{n,\ell}(r)\Omega(r)dr, \tag{1}$$

where we have assumed spherical symmetry, R is the stellar radius and $K_{n,\ell}(r)$ are the rotation kernels. We neglect here the departure from spherical symmetry as it is unlikely to be measured from the limited set of data available here, although other studies (Benomar et al. 2018; Hatta et al. 2019; Bazot et al. 2019) have mentioned it in main-sequence stars. The rotation splittings are taken from Tables 3–8 in Deheuvels et al. (2014).

3. SOLA Rotation inversions

3.1. Formalism and definitions

In their paper, Deheuvels et al. (2014) carried out MOLA inversions to determine the rotation of the stellar core. As a sanity check of the models and kernels, we verified that SOLA inversions provided the same results. The difference between MOLA and SOLA inversions resides in the cost function, which uses a substractive formulation of the term responsible for fitting the averaging kernel to the cost function instead of a multiplicative formulation. In practice SOLA should be slightly less efficient at localising information but more stable and avoid oscillatory wings in the averaging kernels (Pijpers & Thompson 1994; Sekii 1997; Reese 2018; Buldgen et al. 2022). We briefly recall here the properties of the SOLA inversion.

The SOLA cost function writes

$$J(c_k(r_t)) = \int_0^R \left(T(r_t,r) - K_{\rm Avg}(r_t,r)\right)^2 dr + \tan\theta \frac{\sum_{k=1}^N (c_k(r_t)\sigma_k)}{\langle\sigma^2\rangle} + \lambda\left(1 - \int_0^R K_{\rm Avg}(r_t,r)dr\right), \tag{2}$$

with $c_k(r_t)$ the inversion coefficient associated with r_t, the target coordinate of the inversion, $T(r_t,r)$ the target function of the inversion, θ a trade-off parameter to balance the contribution of the observed uncertainties with respect to the fit of the target function, λ is a Lagrange multiplier used to ensure the normalisation of the averaging kernel, $K_{\rm Avg}(r_t,r)$, defined as

$$K_{\rm Avg}(r_t,r) = \sum_{k=1}^N c_k(r_t)K_\Omega(r), \tag{3}$$

and $\langle\sigma^2\rangle = \sum_{k=1}^N \frac{\sigma_k^2}{N}$. The target function is taken here as a Gaussian of the form

$$T(r_t,r) = Ar\exp\left(-\left(\frac{r-r_t}{\Delta c(r_t)} - \frac{\Delta c(r_t)}{2r_t}\right)^2\right), \tag{4}$$

with Δ the width of the Gaussian that is a free parameter and $c(r_t)$ the adiabatic sound speed at the target point of the inversion. This form of target function was defined in Rabello-Soares et al. (1999) in the context of helioseismic inversions.

3.2. Application to Kepler subgiants

As discussed in Sekii (1997), OLA and RLS inversions have a complementary way of analysing the data, and therefore their agreement can be seen as a sign of robustness of the inversion result. Both RLS and MOLA were used in Deheuvels et al. (2014) to determine the rotation of the subgiants studied here. We chose to use SOLA with r_t placed at 0.01R and 0.99R, with R the photospheric radius. Given the limited set of splittings and the low degree of the modes, it would be overly optimistic to attempt an inversion of intermediate layers and we restrict ourselves to the core and outermost layers. As noted by Deheuvels et al. (2014), there can be a pollution of the results of the envelope by the core, but this was measured to be negligible, with the exception of star F. For star E, there are two splittings

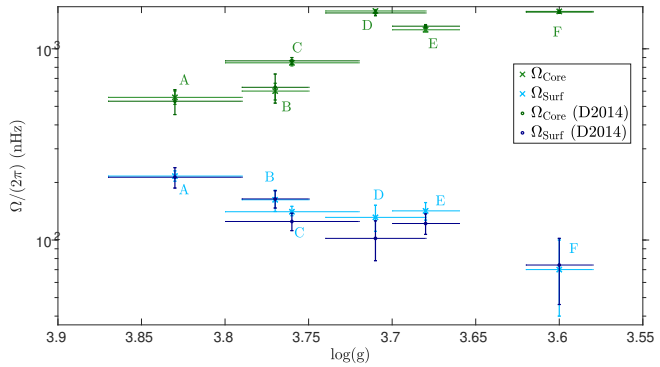

Fig. 1. SOLA inversions results for the core and surface rotations of all stars in the *Kepler* set.

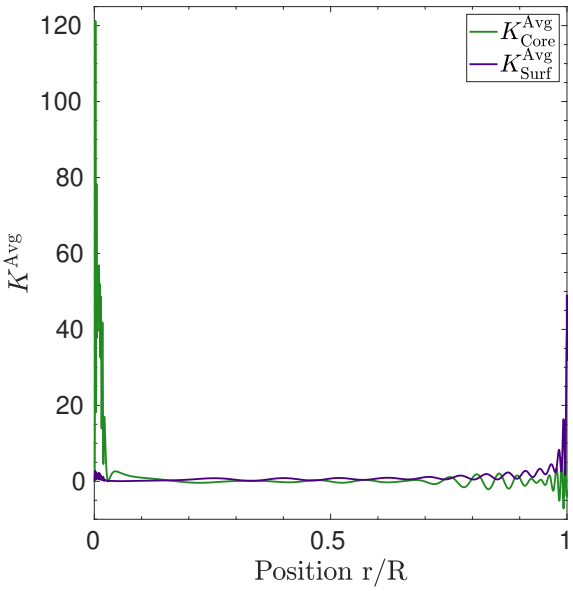

Fig. 2. Averaging kernel for the case of Star C for the core rotation (green) and surface rotation (purple) as a function of the normalised radius.

that were not used for the inversion, namely those at 670 and 698 μHz as they were deemed unreliable by Deheuvels et al. (2014).

Our results are illustrated in Fig. 1 and are compatible with the findings of Deheuvels et al. (2014) using MOLA. We note however that the SOLA inversion was in some cases more unstable and could lead to slightly different results depending on the chosen width of the target function and trade-off parameters for the errors. This was associated with a strong oscillatory behaviour in the core layers, underlining the sensitivity of the surface rotation inference to that of the core. We illustrate in Fig. 2 the averaging kernels for the inner and outermost layers of Star C, as can be seen, some residual oscillations are present at the source when inferring the core rotation, while some signal also remains in the core when inferring the surface rotation. This underlines the difficulties of using such a limited set of splittings, which may lead to some biases in the inversion results, as well as high sensitivity to the trade-off parameters since the illustrated oscillations might vary in amplitude rapidly when changing these parameters.

4. Inversions of Markov chain Monte Carlo rotation

The background of MCMC inversions was first laid out by Fellay et al. (2021) with an application to Kepler 56, and it was independently applied by Hatta et al. (2022) to KIC11145123. As mentioned above, Wilson et al. (2023) have applied this approach to star A of the set, including surface rotation constraints from García et al. (2014) for this particular star. They favoured a transition at about 0.2 stellar radii when this additional information was included. However, as shown in Fig. 7 from Deheuvels et al. (2014), star A is a difficult case for which to attempt these inversions as the precision on the observed splittings is unfortunately quite low. Additionaly, Wilson et al. (2023) did not test multiple forms of the internal rotation profile and only tested a two-zone model.

4.1. Theoretical framework and application to artifical data

The MCMC inversion is based on the approach developed in Fellay et al. (2021), where the Monte Carlo Markov chain algorithm is used to optimise the free parameters of parametric rotation profiles injected in Eq. 1. For each walker, the splittings are evaluated at each step using Eq. 1 and the likelihood of the model is computed following

$$\mathcal{L} = -\frac{1}{2}\chi^2, \tag{5}$$

with

$$\chi^2 = \sum_{k=1}^{N}\left(\frac{\delta\nu_{Th,k} - \delta\nu_{Obs,k}}{\sigma_k}\right)^2, \tag{6}$$

with $\delta\nu_{Obs,k}$ the observed rotation splitting, $\delta\nu_{Th,k}$ the theoretical splitting generated from the parametric profile for a given set of parameters, and σ_k the one sigma uncertainty on the observed splittings.

We then computed the Bayesian information criterion (BIC),

$$\mathrm{BIC} = k\ln(n) - 2\hat{\mathcal{L}}, \tag{7}$$

with k the number of free parameters, n the number of constraints, and $\hat{\mathcal{L}}$ the maximum likelihood.

We used 40 walkers with 2500 iterations after 300 burn-in iterations. Given the high level of degeneracy in the parameter space, we used parallel tempering with six temperatures (see e.g. Gelman et al. 2013, for an introduction to MCMC techniques). The results correspond to the median of the distributions of the parameters, and the errors are the first 15.9% and 84.1%. We followed the guidelines of Foreman-Mackey et al. (2013), according to which the number of iterations should be at least 50 times larger than the autocorrelation of the results for all runs presented here.

We start by presenting the five parametric rotation profiles we considered in our study. We assumed uniform priors on all free parameters of these profiles. For the core and surface rotations, we assumed uniform priors centred around the values from the SOLA inversions, allowing for 4σ variations (with the surface rotation always assumed positive, i.e. rejecting counter-rotating solutions for the surface). For parameters denoting transitions in rotation, we enforced that the transition was located between $[0, 1]$ in normalised radius. For the power-law parameters, denoted α, we enforced it to be between $[0, 40]$. We recall that theoretical predictions for this parameter suggest a value between 1 and 1.5. From their mathematical definitions, it is clear that some more complex parametrisations may degenerate into simpler ones for other parameter values.

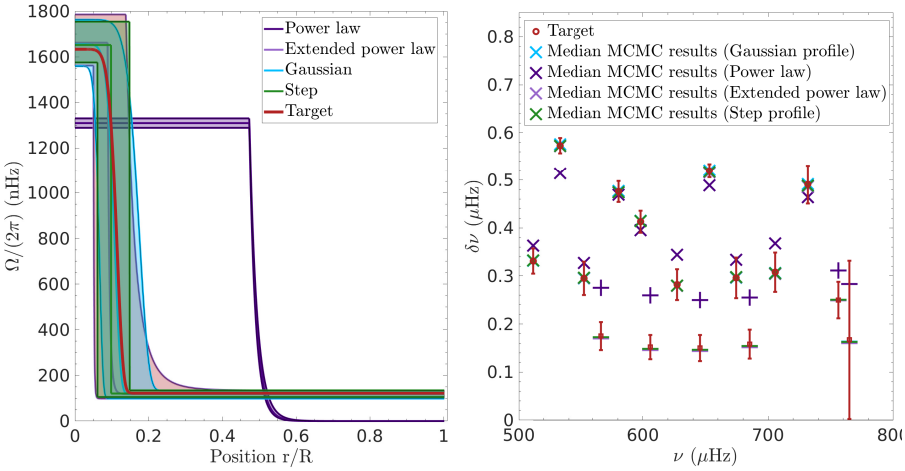

Fig. 3. Recovery test for the MCMC method using the model and dataset of star B. *Left panel:* Recovered rotation profiles as a function of normalised radius. The shaded area provides the 1σ uncertainties on the inferred profiles, and the target is plotted in light purple. *Right panel:* Rotation splittings as a function of frequency for the model of star B (circles indicate dipolar modes, and squares show quadrupolar modes), using the simulated profile illustrated in light purple in the left panel.

4.1.1. Step rotation profile

The first rotation profile we considered was a simple two-zone model, defined by

$$\Omega(r) = \Omega_c, \quad (\text{if } r < 10^{\mathrm{t}})$$
$$\Omega(r) = \Omega_s, \tag{8}$$

with Ω_c, Ω_s, and t the three free parameters of the profile characterising the rotation in the inner layers, the rotation in the outer layers, and the transition between the two zones, respectively. An exponent formulation for the parameter used to localise the transition was used here to avoid boundary effects in the distributions that lead to artefacts due to the physical constraint on $r_t > 0$, which may cause walkers to pile up at the border of the domain.

4.1.2. Gaussian profile

The third profile was the Gaussian profile used in Fellay et al. (2021), which is defined as

$$\Omega(r) = (\Omega_c - \Omega_s) \exp\left(-\left(r_n \times 10^{\mathrm{t}}\right)^{\beta}\right) + \Omega_s, \tag{9}$$

with $r_n = 0.02$ taken as a normalisation constant linked with the peak of the Brunt-Väisälä frequency, Ω_c is the core rotation and Ω_s the surface rotation, and σ is a multipicative factor assigning the location of the transition in rotation. β was taken as a constant in the MCMC runs and was fixed to 8 in Fellay et al. (2021), but in some of the following cases, we changed its value to test smoother or sharper transitions. This profile is thought to be able to mimic the transitions obtained from magnetic instabilities, or at the very least, angular momentum transport processes whose efficiency is inhibited by mean molecular weight gradients. This profile has three free parameters: Ω_c, Ω_s, and t.

4.1.3. Power-law profile

The fourth profile was defined by

$$\Omega(r) = \Omega_c, \quad (\text{if } r < r_{\mathrm{BCE}})$$
$$\Omega(r) = \Omega_c \left(\frac{r_{\mathrm{BCE}}}{r}\right)^{\alpha}, \tag{10}$$

with r_{BCE} the position of the base of the convective envelope, ω_c the core rotation, and α a free parameter constraining the decrease in the rotation towards the surface. This profile had two free parameters.

4.1.4. Extended power-law profile

The fifth parametric profile was an extended version of the power law, defined as

$$\Omega(r) = \Omega_c, \quad (\text{if } r < 10^{\mathrm{t}})$$
$$\Omega(r) = \Omega_c + \Omega_t \left(\left(\frac{10^{\mathrm{t}}}{r}\right)^{\alpha} - 1\right), \tag{11}$$

with Ω_c the core rotation, t linked with the location of the transition from the constant to the power-law rotation profile, α describes the power-law decline of the rotation profile, and Ω_t is the difference between the core rotation Ω_c and the surface rotation that is reached in the upper layers. This rotation profile had four free parameters and was tailored to reach a non-zero surface rotation of $\Omega_c - \Omega_t$.

4.1.5. Test cases on artificial data

We started by testing the robustness of the inferences on artificial data. As already noted in Deheuvels et al. (2014), the data quality is not equivalent for all the stars, and it is also clear that a higher contrast in the profile leads to an easier fit. To determine the potential and possible limitations of our method, we used the models of stars B, D, and E, assumed a parametric rotation profile, and checked the recovery capabilities of the MCMC with the same set of rotation splittings and uncertainties as in the observed case. These tests thus serve as a good example of the capabilities of the technique and can be indicative of intrinsic limitations.

We illustrate the results for star B in Fig. 3, where we have plotted the actual simulated rotation profile andthe recovered median profiles from the MCMC. The splittings are well fit, and the target profiles, indicated in purple, are quite well recovered. We note that attempts were made with for star B with more complex rotation profiles (e.g. a three-zone model), which led to rather poor results. It should also be noted that the rotation contrast is relatively high, which makes it easier to determine trends for the method. Nevertheless, this shows that star B is already a promising target for which to attempt MCMC inversions like this. Moreover, the power-law profile does not recover the observed trends at all and leads to a poor fit of the rotation

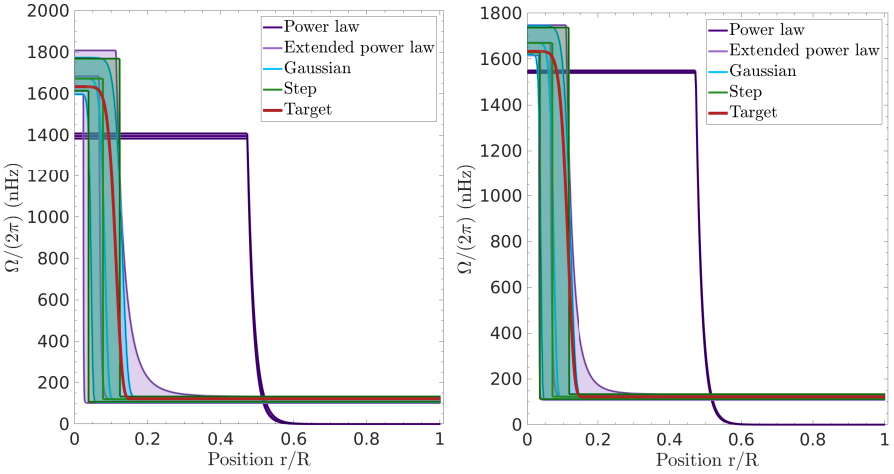

Fig. 4. Recovery test for the MCMC method using the model and dataset of stars D and E. *Left panel:* Recovered rotation profiles as a function of normalised radius for star D. The shaded area provides the 1σ uncertainties on the inferred profiles, and the target is plotted in light purple. *Right panel:* Same for star E.

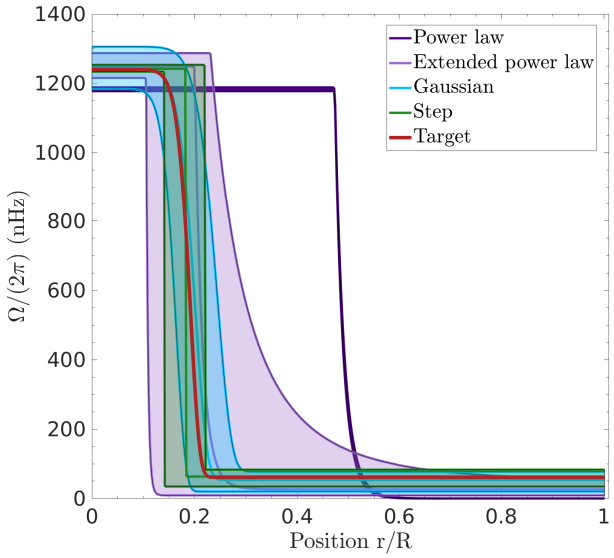

Fig. 5. Recovery test for the MCMC method using the model and dataset of star E using a target profile with a transition in rotation located higher in the star.

splittings. In other words, it is impossible for a power-law profile to reproduce the splittings of a profile with a transition in the radiative layers as the shape of the assumed profile is incompatible with that of the target. All other profiles are able to reproduce the splittings, recover the main trends in the rotation profile, and provide an approximate location of the transition in rotation.

The situation is similar for stars D and E, as illustrated in Fig. 4. In both cases, the method is able to determine the trends of the profile. Even when analytical expressions of the actual target profile and the assumed profile for the MCMC are significantly different, the localisation of the transition is relatively accurate. This gives us confidence that some useful information about the properties of the rotation profile can be extracted, keeping in mind that there is an intrinsic limitation of how many free parameters can be used to describe the profile given the limited amount of data. For the sake of completeness, we also tested a simulated profile for star E, with a transition in rotation located at a higher position in the star. This is illustrated in Fig. 5. One important outcome is that a high transition uncorrelated with the peak of the Brunt-Väisälä frequency is clearly distinguished from a deep transition close to the region of strong chemical gradients.

4.2. Application to observed data and constraints on the internal rotation profile

The previous section showed that the MCMC inversion can provide meaningful constraints on the shape of the internal rotation of the *Kepler* subgiants. Although the case of younger stars seems more difficult, stars D, E, and F still seem promising. We summarise in Figs. 6–8 the results of the MCMC inversion for each star, and Figs. A.1–A.3 in Appendix A show the agreement with the observed splittings we reached. Some distributions for the parameters of the rotation profile are illustrated in the Appendix B for the Gaussian, step, and extended power-law profile. Table 2 summarises our results.

A clear result in all cases is that the rotation profile following the expected properties of large-scale fossil fields as in Kissin & Thompson (2015) (a power-law-style profile with $\alpha \in [1.0, 1.5]$) does not provide a good agreement with the rotation splittings. This is directly seen from the BIC values in Table 2 for stars D, E, and F. For stars A, B, and C, a lower BIC is reached, but for the values of the α parameter that control the stiffness of the power law much higher than 1.5, which is well above the allowed theoretical range from Kissin & Thompson (2015). These results show the importance of taking into account a detailed description of the internal rotation profile and directly extracting the rotation splitting for a given star. Takahashi & Langer (2021) provided a relatively good agreement with the results from Deheuvels et al. (2014) when they tried to reproduce the core and surface rotation of the stars (see their Fig. 12). Here, we show that when the models that reproduce the full-oscillation spectrum are used directly and the rotational splittings are simulated, the agreement is poor. For values of α between 1.0 and 1.5, as prescribed from a theoretical point of view, the fitting of the splitting is very poor for all stars. When the values of α in Eq. 10 are not constrained, the profile always converges on a strong transition and very slow, unphysical, surface rotation, but still does not provide an adequate fit for the splittings of the most p-dominated modes. This implies that the transition is likely below the base of the convective zone, in the radiative interior, to allow to reproduce the splittings of the p-dominated modes without requiring extremely low surface rotation values.

The second conclusion that we can draw is that a deep transition is not clearly favoured in the young subgiants either, but this is to be taken with caution because its localisation is quite challenging. It should also be noted that star B shows some unusual behaviour in the splittings, with some dipolar modes showing higher splitting values than the quadrupolar ones even at a similar coupling level. This leads to some difficulties in

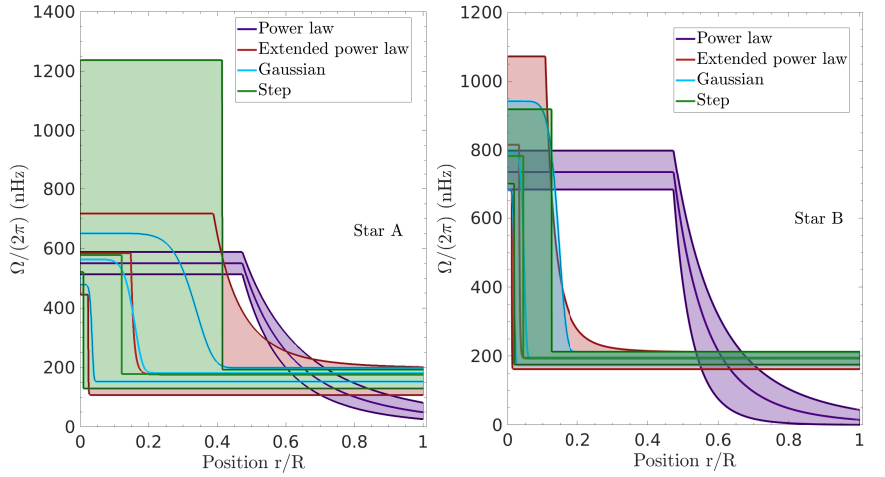

Fig. 6. Inferred rotation profile as a function of normalised radius for stars A and B using the MCMC inversion technique and the various parametrised profiles of Sect. 4.1. The shaded areas show 1σ uncertainties on the inferred profiles. *Left panel:* Case of star A. *Right panel:* Case of star B.

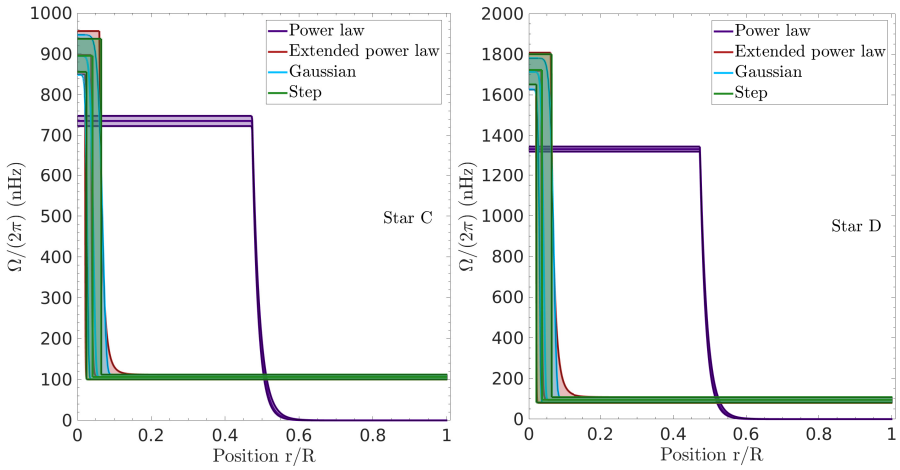

Fig. 7. Same as Fig. 6 for stars C (*left panel*) and D (*right panel*).

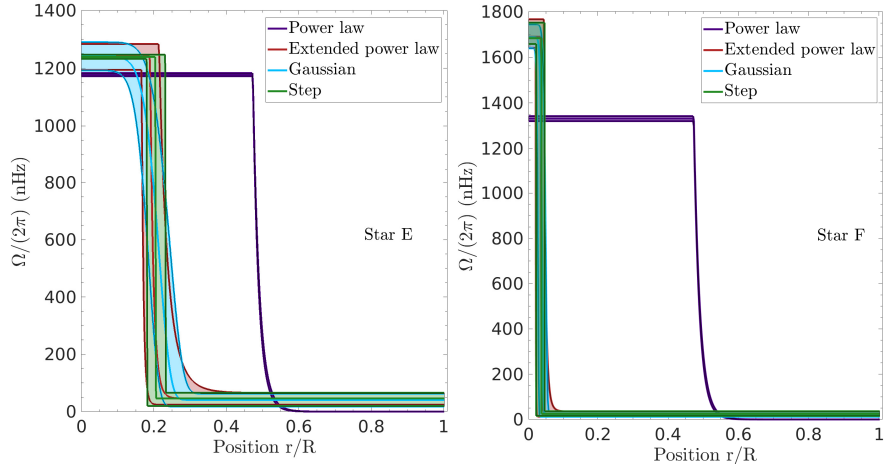

Fig. 8. Same as Fig. 6 for stars E (*left panel*) and F (*right panel*).

reproducing the splittings. This behaviour is not observed in other stars, although some splittings in stars C and D show a similar behaviour. It is unclear whether this is a result of the forward modelling procedure we used to determine the properties of the evolution model, which could affect the coupling, or if it is caused by some physical behaviour in the rotation profile (e.g. latitudinal differential rotation or a more slowly rotating core) that the inversion is unable to determine.

The more evolved subgiants show some more interesting features, with the lower-mass range (stars C, D, and F) showing a location of the rotation transition close to (but not exactly at) the position of the peak in the Brunt-Väisälä frequency, which is in line with previous results (Di Mauro et al. 2016, 2018; Fellay et al. 2021). This is illustrated in Figs. 9 and 10, which show the position of the median profile and the best-fit profile against the Brunt-Väisälä frequency profile for stars C, D, E, and F. Namely, the transition in rotation is linked with the position in the star where the effects of mean molecular weight gradients seem to dominate. This is in line with both the effects of magnetic instabilities and internal gravity waves. Star E, however, the most

Table 2. Median parameter values determined for each star from our MCMC inversion.

Name		Star A	Star B	Star C	Star D	Star E	Star F
Gaussian	t	$0.91^{+0.32}_{-0.66}$	$0.44^{+0.32}_{-0.28}$	$0.32^{+0.28}_{-0.29}$	$0.32^{+0.22}_{-0.15}$	$1.01^{+0.10}_{-0.09}$	$0.29^{+0.11}_{-0.16}$
	Ω_s	181^{+17}_{-29}	175^{+14}_{-20}	118^{+6}_{-6}	95^{+12}_{-14}	55^{+23}_{-38}	24^{+12}_{-12}
	Ω_c	563^{+70}_{-56}	825^{+75}_{-68}	877^{+78}_{-45}	1618^{+54}_{-73}	1185^{+27}_{-27}	1664^{+45}_{-37}
	BIC	16.59	25.27	48.57	33.13	31.63	16.09
Step	t	$-0.92^{+0.54}_{-1.12}$	$-1.46^{+0.45}_{-0.53}$	$-1.43^{+0.30}_{-0.20}$	$-1.44^{+0.24}_{-0.24}$	$-0.74^{+0.06}_{-0.06}$	$-1.43^{+0.10}_{-0.23}$
	Ω_s	177^{+15}_{-48}	176^{+13}_{-17}	123^{+6}_{-7}	95^{+13}_{-13}	65^{+17}_{-28}	25^{+11}_{-9}
	Ω_c	577^{+646}_{-57}	861^{+160}_{-76}	892^{+50}_{-43}	1723^{+77}_{-71}	1237^{+8}_{-8}	1684^{+67}_{-26}
	BIC	14.69	22.45	45.91	30.21	28.49	13.10
Power Law	α	$3.22^{+0.76}_{-0.58}$	$10.8^{+12}_{-3.3}$	$26.2^{+2.7}_{-4.4}$	$28.2^{+2.0}_{-3.0}$	$28.7^{+1.0}_{-2.0}$	$29^{+0.7}_{-1.5}$
	Ω_c	551^{+71}_{-38}	795^{+33}_{-45}	746^{+12}_{-13}	1333^{+12}_{-13}	1180^{+6}_{-6}	1331^{+11}_{-11}
	BIC	15.14	28.55	48.34	164.55	220.27	326.05
Power Law Var	r_t	$-0.83^{+0.42}_{-0.81}$	$-1.43^{+0.45}_{-0.47}$	$-1.53^{+0.28}_{-0.25}$	$-1.47^{+0.24}_{-0.24}$	$-0.75^{+0.10}_{-0.08}$	$-1.46^{+0.10}_{-0.23}$
	α	19^{+14}_{-14}	18^{+15}_{-14}	-20.0^{+13}_{-14}	-20.0^{+13}_{-14}	-20.0^{+14}_{-13}	-21.0^{+14}_{-12}
	Ω_s	176^{+21}_{-70}	113^{+32}_{-71}	123^{+6}_{-8}	94^{+15}_{-14}	58^{+21}_{-37}	23^{+12}_{-11}
	Ω_c	407^{+113}_{-70}	680^{+214}_{-82}	781^{+100}_{-49}	1624^{+76}_{-78}	1181^{+40}_{-16}	1667^{+54}_{-38}
	BIC	21.12	28.29	50.74	35.65	34.20	18.52

massive of the sample, shows a transition in rotation that is clearly unrelated with the location of the chemical composition gradient and is in fact much higher in relative radius than any other star. We emphasise that these conclusions can be drawn from multiple parametrisations of the profile, some of which allow for smooth transitions within the radiative zone. A smooth transition like this is not favoured in all cases, but it is unclear whether this is due to a lack of constraints in the splittings or to an actual feature of the rotation profile. It is also clear that these are azimuthally averaged profiles and do not imply that some breaking from spherical symmetry does not occur in these stars.

5. Discussion

The properties of the inferred profiles allow us to draw a more general picture and discuss some additional perspectives. Our inversion results clearly invalidate fossil magnetic fields in the whole radiative region, as theorised by Kissin & Thompson (2015) and tested by Takahashi & Langer (2021). We thus confirm the results obtained by Fellay et al. (2021) using the same approach for Kepler 56, which invalidated this shape for the internal rotation profile, even with a high value for the α parameter in the power-law rotation profile.

However, it is still difficult to draw a full picture of the evolutionary trends in the rotation profile of the sample of subgiants from our results alone. For example, the case of stars A and B is somewhat problematic, with difficulties in localising the transition in rotation, although it indicates a transition that is disconnected from the peak in the Brunt-Väisälä frequency or a smoother transition over an extended region. We also note some difficulties in reproducing all splittings for the case of star B. For star C, a better localisation is achieved, although two splittings seem to be difficult to reproduce. This perhaps also calls for a detailed remodelling of this star.

For the more evolved subgiants, a different picture can be drawn. The lower-mass stars appear to show a rotation transition that is linked with the chemical composition gradients, which is in line with the results of Di Mauro et al. (2016), Di Mauro et al. (2018) and Fellay et al. (2021). Star E, however, the more massive star, has a transition much higher, at about 28% of the total mass, while the maximum extension of the convective core on the main sequence is around twice lower. Whether this implies the presence of magnetic fields generated in the convective core that remain as a fossil fields in these layers is unclear and requires input from simulations regarding the survival of these fields and their confinement. This positioning of the transition is robust, however, and was confirmed with various parametrisations as well as with artificial data.

However, we caution that these observations cannot be generalised. The number of targets must be increased and a detailed modelling of the two stars in Deheuvels et al. (2014) and Deheuvels et al. (2020) is required for a clearer picture of the evolutionary trends. Star C appears to favour a transition close to the peak of the Brunt-Väisälä frequency, while star A does not. In this respect, young subgiants appear to be the key for unravelling the physical nature of the angular momentum transport during the late main sequence because the key difference between magnetic instabilities and internal gravity waves is the rotation of the deep core. Internal gravity waves are indeed expected to induce a more slowly rotating core, which is in line with Deheuvels et al. (2020), while magnetic instabilities, even in their most efficiently calibrated form (Fuller et al. 2019), can enforce solid-body rotation at best. A combination of this with detailed investigations of some red giant branch targets might also prove useful to provide a picture of the changes in the shape of the rotation profile as the star evolves, and thus, to constrain the properties of the missing angular momentum transport.

A strong limitation of our inference results is the 1D structure of the profile. It is thus entirely possible than azimuthal patterns could be present and are not seen by the inversion procedure. These effects need to be treated in a forward approach, with direct input from simulations that are averaged to determine the rotation splittings they would generate, in a similar fashion to what is done with entrainment laws derived from convective simulations.

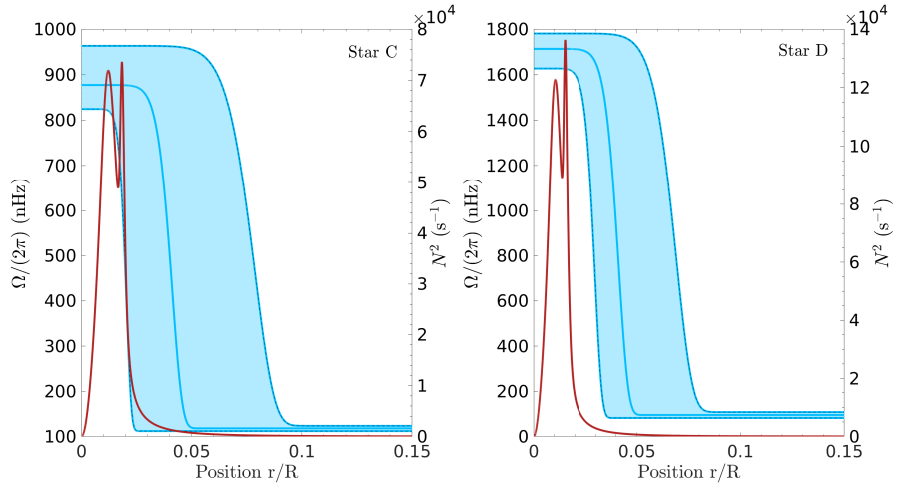

Fig. 9. Comparison of the location of the transition in rotation (left y-axis) with the Brunt-Väisälä frequency profile (right y-axis) for stars C (*left panel*) and D (*right panel*).

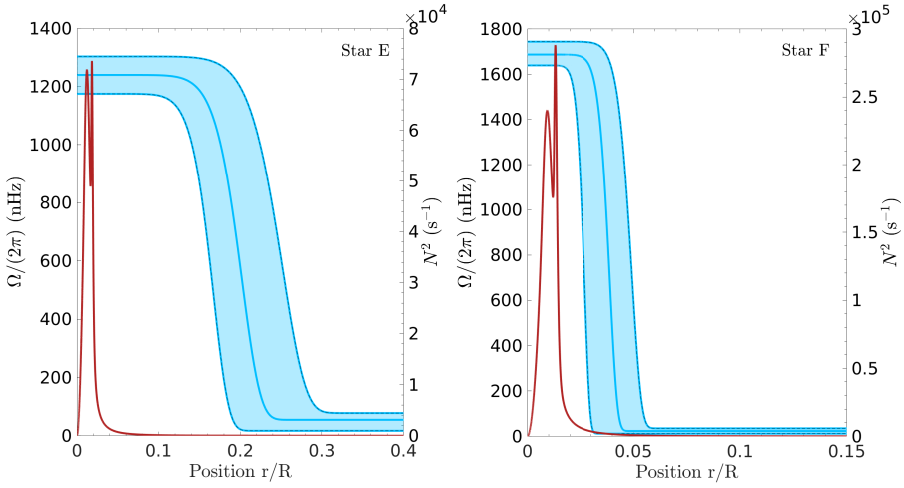

Fig. 10. Same as Fig. 9, but for stars E and F.

6. Conclusion

We have analysed the rotation properties of the six subgiants studied in Deheuvels et al. (2014) in detail. We confirmed their results based on MOLA and RLS inversion techniques by carrying out SOLA inversions and supplemented these approaches with MCMC inversions, following Fellay et al. (2021) and Hatta et al. (2022). Using artificial data with the same uncertainties as the actual observations, we demonstrated that our MCMC rotation inversion is able to recover some useful information about the internal rotation profile of these stars. We thus showed that some major characteristics were accessible, such as the core and surface rotation, as well as the location of the transition in rotation, using the same sets of modes and given uncertainties as in the observed cases, even though the profiles did not exactly match those of the target. We also showed that there is a clear intrinsic limitation to the number of parameters that could be used to describe the profiles, namely about three, and that the younger stars in the sample were more difficult to work with.

When applied to the observed targets, the MCMC inversion provides values that are compatible with those inferred with the SOLA inversion. Stars C, D, and F show a transition in rotation that is compatible with the position of the core transition, where the mean molecular weight gradients are expected to dominate the Brunt-Väisälä frequency profile. Stars A and B do not show such clear signs, but this could be due to the lower precision in the observed splittings for star A and to the difficulty of reproducing the observed splittings for star B. Whether this is due to an issue in the forward-modelling procedure we used to determine the evolution model or if the parametrisation is unsuitable requires further analysis. For star E, the transition in rotation is clearly localised and uncorrelated with the position of the mean molecular weight peak in the Brunt-Väisälä profile. Surprisingly, this star is also the most massive of the sample, and the location of the transition is also of the same order of magnitude as the expected extension of the convective core during the main sequence.

Another clear conclusion from our study is that the solution suggested by Kissin & Thompson (2015) and tested by Takahashi & Langer (2021) is incompatible when a detailed comparison of the rotation splittings is made. This further confirms the findings of Di Mauro et al. (2016, 2018), and Fellay et al. (2021).

Our findings seem to indicate that a diverse behaviour may be expected to explain the rotation properties of subgiants and red giants. A consistent remodelling of the younger stars in the sample and a joint analysis of MCMC inversions including the young subgiants of Deheuvels et al. (2020) will also be very informative, as these stars seem to favour internal gravity waves as the efficient transport mechanism acting after the main sequence (Pinçon et al. 2017). A full reanalysis like this will be done in a future study. An increased set of targets for which these inferences can be achieved would also be extremely constraining on the physical nature of the angular momentum

transport process. This will be achieved with the future PLATO mission (Rauer et al. 2014), which is expected to deliver high-quality seismic data for thousands of subgiant stars (Goupil et al. 2024). An important aspect of constraining angular momentum on the main-sequence would be the detection of gravity modes in F-type stars (Breton et al. 2023) because they would allow us to fill a gap in our probing of internal rotation, as Bétrisey et al. (2023) demonstrated that p-modes are unable to infer the presence of an efficient AM transport process even for the best F-type *Kepler* targets.

Acknowledgements. We thank the anonymous referee for their careful reading of the manuscript. G.B. and J.B. are funded by the SNF AMBIZIONE grant No 185805 (Seismic inversions and modelling of transport processes in stars). G.B. acknowledges funding from the Fonds de la Recherche Scientifique – FNRS. L.F. is supported by the Fonds de la Recherche Scientifique (FNRS) as a Research fellow. S.D. acknowledges support from from the project BEAMING ANR-18-CE31-0001 of the French National Research Agency (ANR) and from the Centre National d'Etudes Spatiales (CNES). M.F. is a Postdoctoral Researcher of the Fonds de la Recherche Scientifique – FNRS. E.F. is support by SNF grant number 200020_212124.

References

Aerts, C., Mathis, S., & Rogers, T. M. 2019, ARA&A, 57, 35
Auvergne, M., Bodin, P., Boisnard, L., et al. 2009, A&A, 506, 411
Bazot, M., Benomar, O., Christensen-Dalsgaard, J., et al. 2019, A&A, 623, A125
Beck, P. G., Montalban, J., Kallinger, T., et al. 2012, Nature, 481, 55
Benomar, O., Bazot, M., Nielsen, M. B., et al. 2018, Science, 361, 1231
Bétrisey, J., Eggenberger, P., Buldgen, G., Benomar, O., & Bazot, M. 2023, A&A, 673, L11
Borucki, W. J., Koch, D., Basri, G., et al. 2010, Science, 327, 977
Breton, S. N., Dhouib, H., García, R. A., et al. 2023, A&A, 679, A104
Buldgen, G., Bétrisey, J., Roxburgh, I. W., Vorontsov, S. V., & Reese, D. R. 2022, Front. Astron. Space Sci., 9, 942373
Charbonnel, C., & Talon, S. 2005, Science, 309, 2189
Christensen-Dalsgaard, J. 2011, Astrophysics Source Code Library [record ascl:1109.002]
Deheuvels, S., García, R. A., Chaplin, W. J., et al. 2012, ApJ, 756, 19
Deheuvels, S., Doğan, G., Goupil, M. J., et al. 2014, A&A, 564, A27
Deheuvels, S., Ballot, J., Beck, P. G., et al. 2015, A&A, 580, A96
Deheuvels, S., Ballot, J., Eggenberger, P., et al. 2020, A&A, 641, A117
Di Mauro, M. P., Ventura, R., Cardini, D., et al. 2016, ApJ, 817, 65
Di Mauro, M. P., Ventura, R., Corsaro, E., & Lustosa De Moura, B. 2018, ApJ, 862, 9
Fellay, L., Buldgen, G., Eggenberger, P., et al. 2021, A&A, 654, A133
Foreman-Mackey, D., Hogg, D. W., Lang, D., & Goodman, J. 2013, PASP, 125, 306
Fuller, J., Piro, A. L., & Jermyn, A. S. 2019, MNRAS, 485, 3661
García, R. A., Ceillier, T., Salabert, D., et al. 2014, A&A, 572, A34
Gehan, C., Mosser, B., Michel, E., Samadi, R., & Kallinger, T. 2018, A&A, 616, A24
Gelman, A., Carlin, J., Stern, H., et al. 2013, Bayesian Data Analysis, Third Edition, Chapman & Hall/CRC Texts in Statistical Science (Taylor & Francis)
Gough, D. O. 1981, MNRAS, 196, 731
Gough, D. O., & McIntyre, M. E. 1998, Nature, 394, 755
Goupil, M. J., Catala, C., Samadi, R., et al. 2024, A&A, 683, A78
Hansen, C. J., Cox, J. P., & van Horn, H. M. 1977, ApJ, 217, 151
Hatta, Y., Sekii, T., Takata, M., & Kurtz, D. W. 2019, ApJ, 871, 135
Hatta, Y., Sekii, T., Benomar, O., & Takata, M. 2022, ApJ, 927, 40
Kissin, Y., & Thompson, C. 2015, ApJ, 808, 35
Maeder, A. 2009, Physics, Formation and Evolution of Rotating Stars (Berlin, Heidelberg: Springer)
Marques, J. P., Goupil, M. J., Lebreton, Y., et al. 2013, A&A, 549, A74
Mosser, B., Goupil, M. J., Belkacem, K., et al. 2012, A&A, 548, A10
Pijpers, F. P., & Thompson, M. J. 1994, A&A, 281, 231
Pinçon, C., Belkacem, K., Goupil, M. J., & Marques, J. P. 2017, A&A, 605, A31
Rabello-Soares, M. C., Basu, S., & Christensen-Dalsgaard, J. 1999, MNRAS, 309, 35
Rauer, H., Catala, C., Aerts, C., et al. 2014, Exp. Astron., 38, 249
Reese, D. R. 2018, Astrophys. Space Sci. Proc., 49, 75
Ricker, G. R., Winn, J. N., Vanderspek, R., et al. 2015, J. Astron. Telescopes Instrum. Syst., 1, 014003
Sekii, T. 1997, in Sounding Solar and Stellar Interiors, eds. J. Provost, & F.-X. Schmider, 181
Spruit, H. C. 2002, A&A, 381, 923
Takahashi, K., & Langer, N. 2021, A&A, 646, A19
Wilson, T. A., Casey, A. R., Mandel, I., et al. 2023, MNRAS, 521, 4122

Appendix A: Additional figures

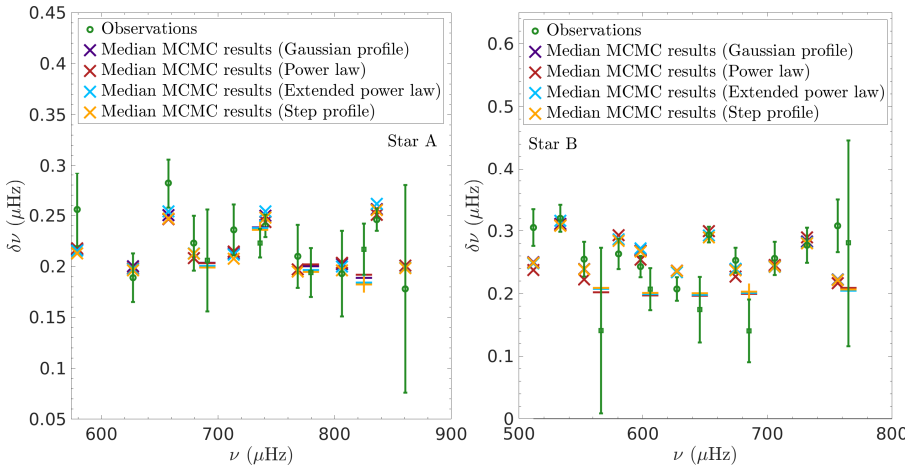

Fig. A.1. Agreement between the inferred rotation splittings for the various median parametric rotation profile and the observations (green) for stars A and B (circles indicate dipolar modes, and squares show quadrupolar modes). *Left panel:* Results for star A. *Right panel:* Results for star B.

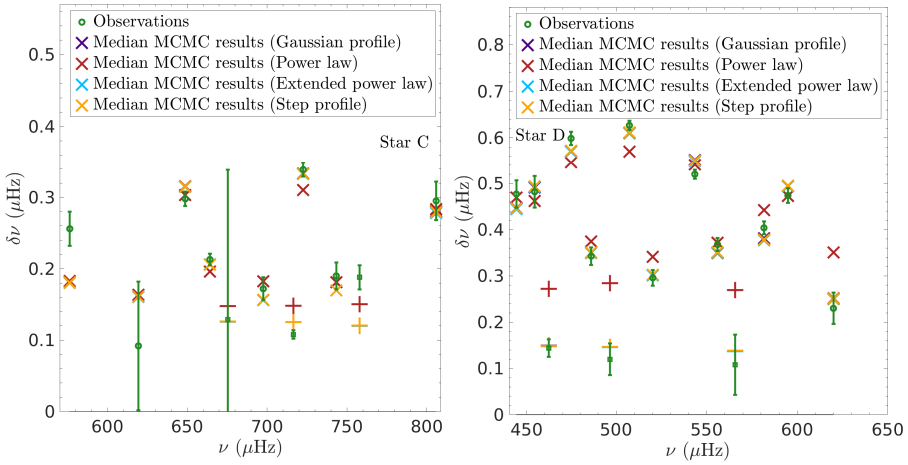

Fig. A.2. Same as Fig. A.1 for stars C (left panel) and D (right panel).

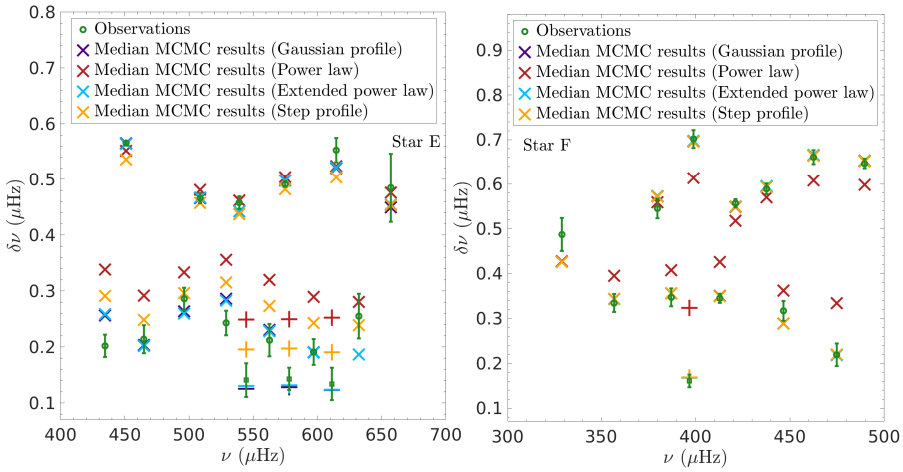

Fig. A.3. Same as Fig. A.1 for stars E (left panel) and F (right panel).

Appendix B: Posterior distributions for the MCMC runs

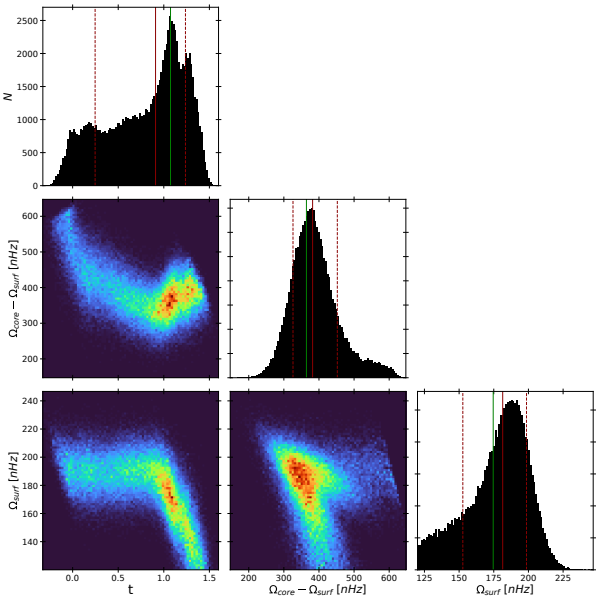

Fig. B.1. Posterior distributions for the MCMC inversion of Star A using the Gaussian rotation profile.

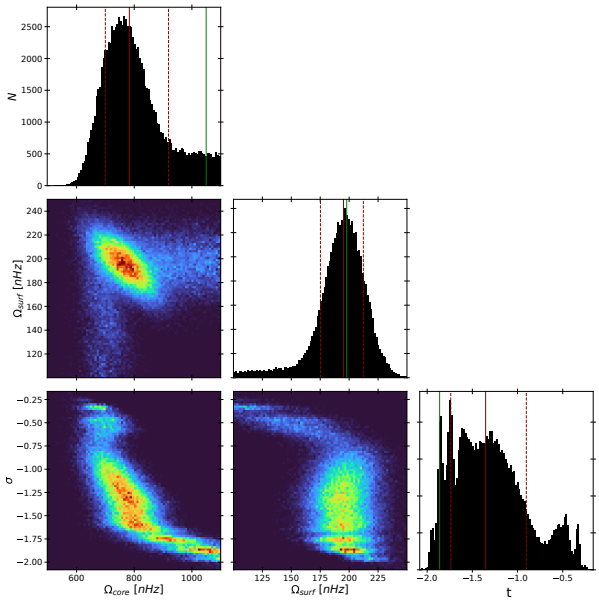

Fig. B.2. Posterior distributions for the MCMC inversion of Star B using the step rotation profile.

In this section, we provide the full posterior distributions of the parameters for the Gaussian profiles for Stars A,D,F, Step profiles for Stars B and E and Extended Power Law parametric profiles for Star C.

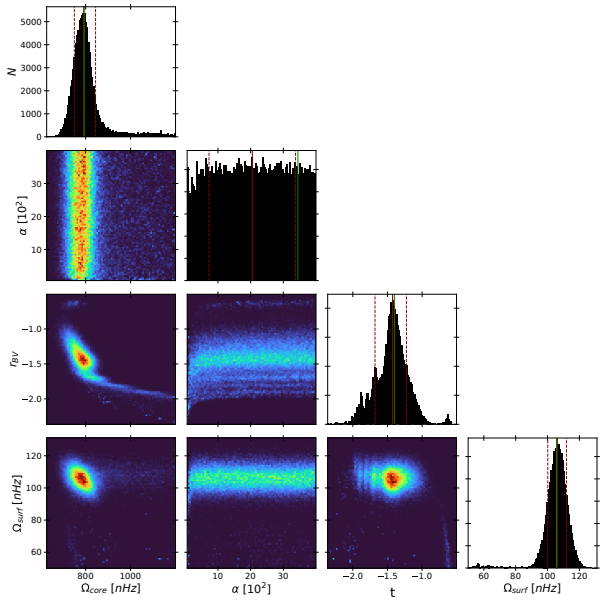

Fig. B.3. Posterior distributions for the MCMC inversion of Star C using the extended power law rotation profile.

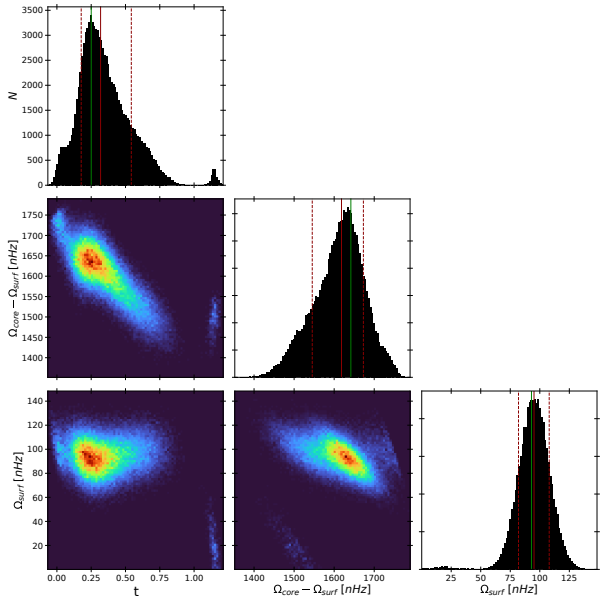

Fig. B.4. Posterior distributions for the MCMC inversion of Star D using the Gaussian rotation profile.

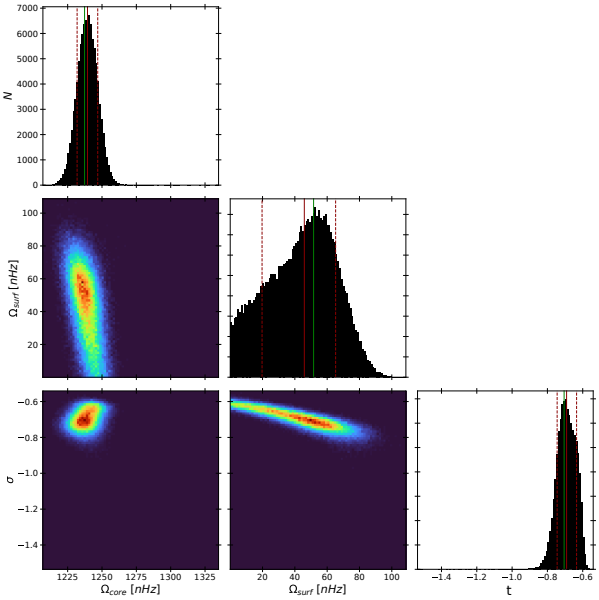

Fig. B.5. Posterior distributions for the MCMC inversion of Star E using the step rotation profile.

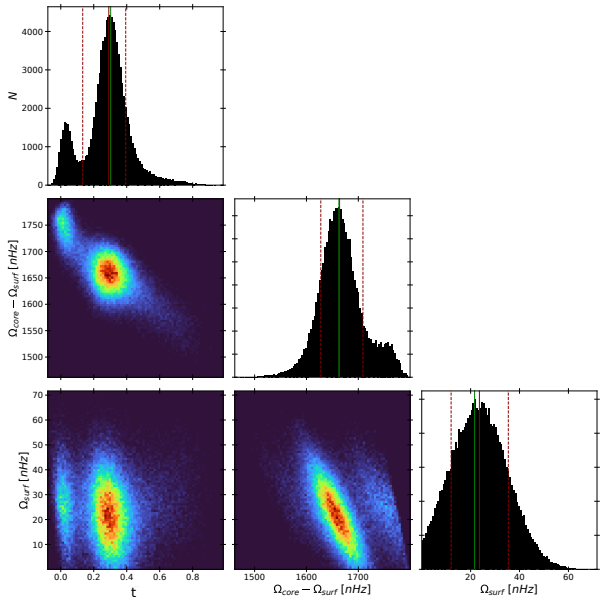

Fig. B.6. Posterior distributions for the MCMC inversion of Star F using the Gaussian rotation profile.